

Neutrophils Defensively Degrade Graphene Oxide in a Lateral Dimension Dependent Manner through Two Distinct Myeloperoxidase Mediated Mechanisms

Shiyi Huang

Shanghai Jiao Tong University

Sijie Li

Shanghai Jiao Tong University

Yanlei Liu

Shanghai Jiao Tong University

Behafarid Ghalandari

Shanghai Jiao Tong University

Ling Hao

George Washington University

Chengjie Huang

Shanghai Jiao Tong University

Wenqiong Su

Shanghai Jiao Tong University <https://orcid.org/0000-0003-4914-346X>

Yuqing Ke

Shanghai Jiao Tong University

Daxiang Cui

Institute of Micro-Nano Science and Technology, School of Electronic Information and Electrical Engineering, Shanghai Jiao Tong University, Shanghai 200240, P. R. China

Xiao Zhi

Shanghai Jiao Tong University

Xianting Ding (✉ dingxianting@sjtu.edu.cn)

Shanghai Jiao Tong University <https://orcid.org/0000-0002-1549-3499>

Article

Keywords: graphene oxide, neutrophils, biodegradation, myeloperoxidase

Posted Date: May 26th, 2021

DOI: <https://doi.org/10.21203/rs.3.rs-517060/v1>

License:  This work is licensed under a Creative Commons Attribution 4.0 International License.

[Read Full License](#)

Neutrophils Defensively Degrade Graphene Oxide in a Lateral Dimension Dependent Manner through Two Distinct Myeloperoxidase Mediated Mechanisms

Shiyi Huang¹, Sijie Li¹, Yanlei Liu², Behafarid Ghalandari¹, Ling Hao³, Chengjie Huang¹, Wenqiong Su¹, Yuqing Ke¹, Daxiang Cui², Xiao Zhi^{1*} and Xianting Ding^{1*}

¹ State Key laboratory of Oncogenes and Related Genes, Institute for Personalized Medicine, School of Biomedical Engineering, Shanghai Jiao Tong University, Shanghai 200030, China

² Shanghai Engineering Center for Intelligent Diagnosis and Treatment Instrument, School of Electronic Information and Electrical Engineering, Shanghai Jiao Tong University, Shanghai 200240, China

³ Department of Chemistry, George Washington University, Washington, D.C., 20052, USA.

* Correspondence to: Xiao Zhi, Ph.D. and Xianting Ding, Ph.D.

Keywords: graphene oxide, neutrophils, biodegradation, myeloperoxidase

Abstract

The boosting exploitation of graphene oxide (GO) increases exposure risk to human beings. However, as the first line defender, neutrophils' mechanism of defensive behavior towards GO invasion remains unclear. Herein, we discover that neutrophils defensively degrade GO in a lateral dimension dependent manner. The micrometer-sized GO (mGO) induces NETosis by releasing neutrophil extracellular traps (NETs), while nanometer-sized GO (nGO) elicits neutrophil degranulation. The neutrophils' defensive behavior is accompanied with generation of reactive oxygen species and activation of p-ERK and p-Akt kinases. We unveil that mGO-induced NETosis is NADPH oxidase (NOX)-independent, while nGO-triggered degranulation is NOX-dependent. Furthermore, myeloperoxidase (MPO) is identified to be a determinant mediator despite distinct neutrophil phenotypes in the biodegradation. Neutrophils release NETs comprising of MPO upon activated with mGO, while MPO is secreted *via* nGO induced-degranulation. Moreover, the binding energy between MPO and GO is calculated to be 69.8728 kJ·mol⁻¹, which indicates that electrostatic interactions mainly cause the spontaneous binding process in a spatial distance of 9.2 Å. Meanwhile, the central enzymatic biodegradation is found to occur at oxygenic active sites and defects on GO. Mass spectrometry analysis deciphers the degradation products are biocompatible molecules like flavonoids and polyphenols. Our study provides fundamental evidence and practical guidance for functional biomaterial development in sustainable nanotechnology, including but not limited to vaccine adjuvant and drug carrier.

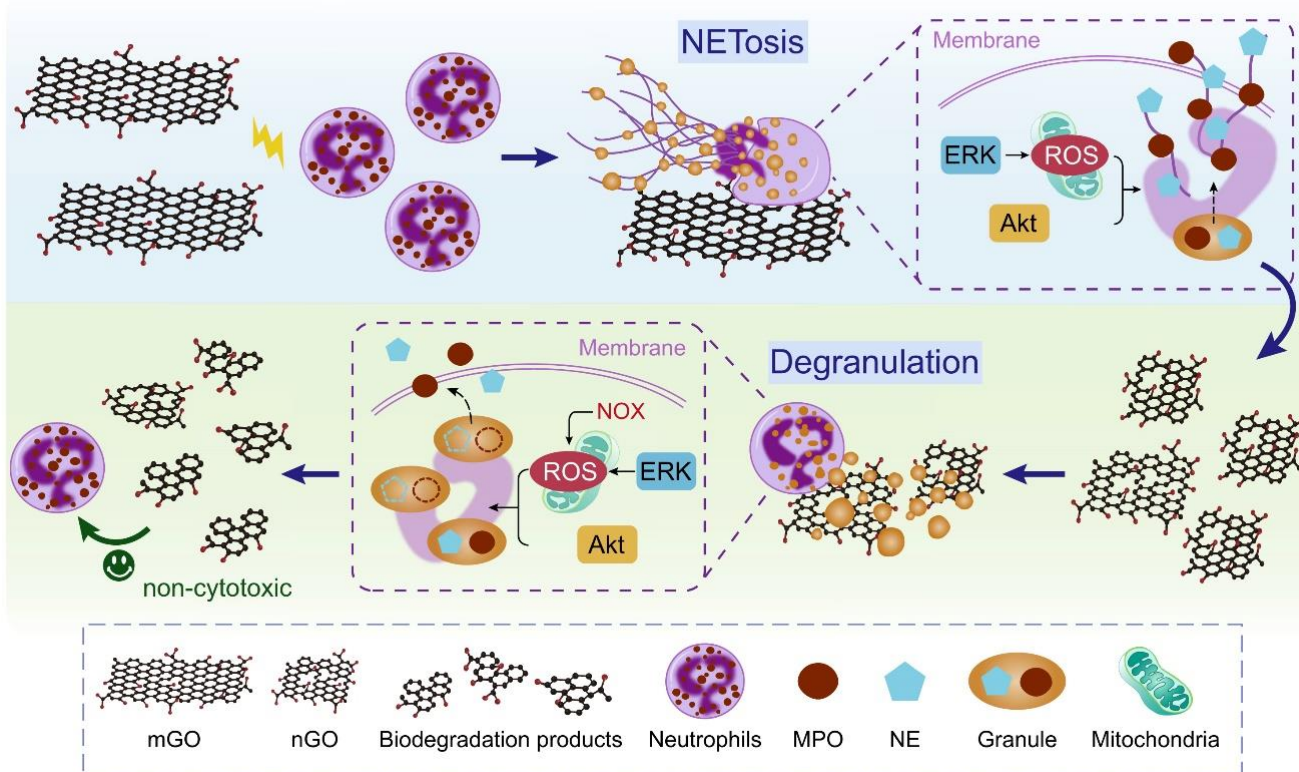
1. Introduction

Graphene oxide (GO), a two-dimensional graphene derivative, possesses hydrophobic sp^2 - and sp^3 -hybridized carbon skeleton and abundant hydrophilic groups (hydroxyl, epoxide, and carboxyl) forming defect sites at its edge and plane.^{1, 2} Such unique structure imparts many fascinating physiochemical properties like large surface area, strong adsorbability, and versatile functionality.³ Hence, GO-based potential applications such as drug delivery,⁴ implanted biodevices,⁵ vaccine adjuvant,⁶ energy storage,⁷ and sea water desalinization⁸ have aroused. Therefore, risk evaluation of GO-based technologies and products requires rigorous characterization.⁹

Immune system provides a universal and immediate defense against foreign invaders.¹⁰ Once GO enters body, it will encounter neutrophils, macrophages and dendritic cells (DCs), which represent the first line of immune system. Several *in vivo* studies indicated that GO elicited cell membrane lipid change of neutrophils,¹¹ promoted size-dependent M1 induction of macrophages,¹² and suppressed antigen presentation by DCs to T cells.¹³ However, the immune effect and cellular mechanism of defensive behavior towards GO invasion are still unraveled.

Neutrophils, as dominant immune cells in quantity, play important roles in immune defense by three major strategies, namely phagocytosis, degranulation, and neutrophils extracellular traps (NETs) *via* 'NETosis' (a specific neutrophil death program).¹⁴ Degranulation of antimicrobial factors involving myeloperoxidase (MPO) leads to destruction of invaders.¹⁵ Besides, neutrophils could directly contact with invaders by forming unique extracellular web-like NETs that compose of decondensed chromatin, and antimicrobials including MPO and neutrophil elastase (NE).¹⁶ MPO is the most abundant heme protein in neutrophils, which catalyzes hydrogen peroxide (H_2O_2) to form hypochlorous acid (HClO) and other oxidants.^{17, 18} NE is a neutrophil-specific serine protease that kills foreign invaders like viruses and bacteria.¹⁹ MPO and NE are stored in azurophilic granules in resting neutrophils, however, they will be released outside the neutrophils cooperatively in response to invaders.¹⁹ In recent years, MPO has been reported in degrading carbon materials like single-walled carbon nanotubes (SWCNTs)²⁰ and GO sheets^{21, 22}. However, the mechanism of GO biodegradation including chemical reaction details, related signaling pathways and fate of neutrophils is not clear.

Herein, we carefully explore the bi-direction interactions between neutrophils and GO, including neutrophils biodegrading GO and GO switching neutrophils' fate (Scheme 1). We unveil that neutrophils autonomously degrade GO in a lateral dimension dependent manner. Micrometer-sized GO (mGO) and nanometer-sized GO (nGO) selectively direct neutrophils to two distinct fates: NETosis or degranulation. Furthermore, the underlying signaling pathways are carefully investigated. Thermodynamics analysis and active sites of GO biodegradation are also elucidated. Ultimately, the biodegradation products of GO are identified and confirmed for their good biocompatibility with neutrophils. Collectively, the complicated interactions between neutrophils and GO are clearly depicted.



Scheme 1. Neutrophils degrade GO in an autonomous manner and lateral dimension dependent manner. Neutrophils release NETs in response to mGO, while induce degranulation in response to nGO. GO sheets are eventually biodegraded into non-cytotoxic small molecules by neutrophils.

2. Results and discussion

2.1. GO is defensively degraded by neutrophils

To address the interactions between neutrophils and GO, GO sheets of different lateral dimension were firstly synthesized by modified Hummers' method as previously described.⁶ The lateral dimension and thickness of mGO and nGO sheets were analyzed by atomic force microscopy (AFM) and transmission electron microscopy (TEM), and recorded as $4.299 \pm 0.824 \mu\text{m}$ and $289.9 \pm 111.7 \text{ nm}$, respectively (Supplementary Fig. 1). Other physicochemical characterizations including surface charge, degree of defects and chemical composition were summarized in Table S1. Then, neutrophils were isolated from mouse bone marrow and incubated with GO at 37 °C. The neutrophils were refreshed every 12 h due to short-life.²³ To facilitate investigating GO and neutrophils respectively, the experiments were performed in Transwell[®] chambers (Supplementary Fig. 2). The permeable membrane pore was small enough to prevent neutrophils phagocytosis and transmigration, but large enough to allow neutrophils to extend filopodia and contact GO on the other side. We removed the Transwell[®] insert after incubation for collecting GO suspension and cells for further analysis.

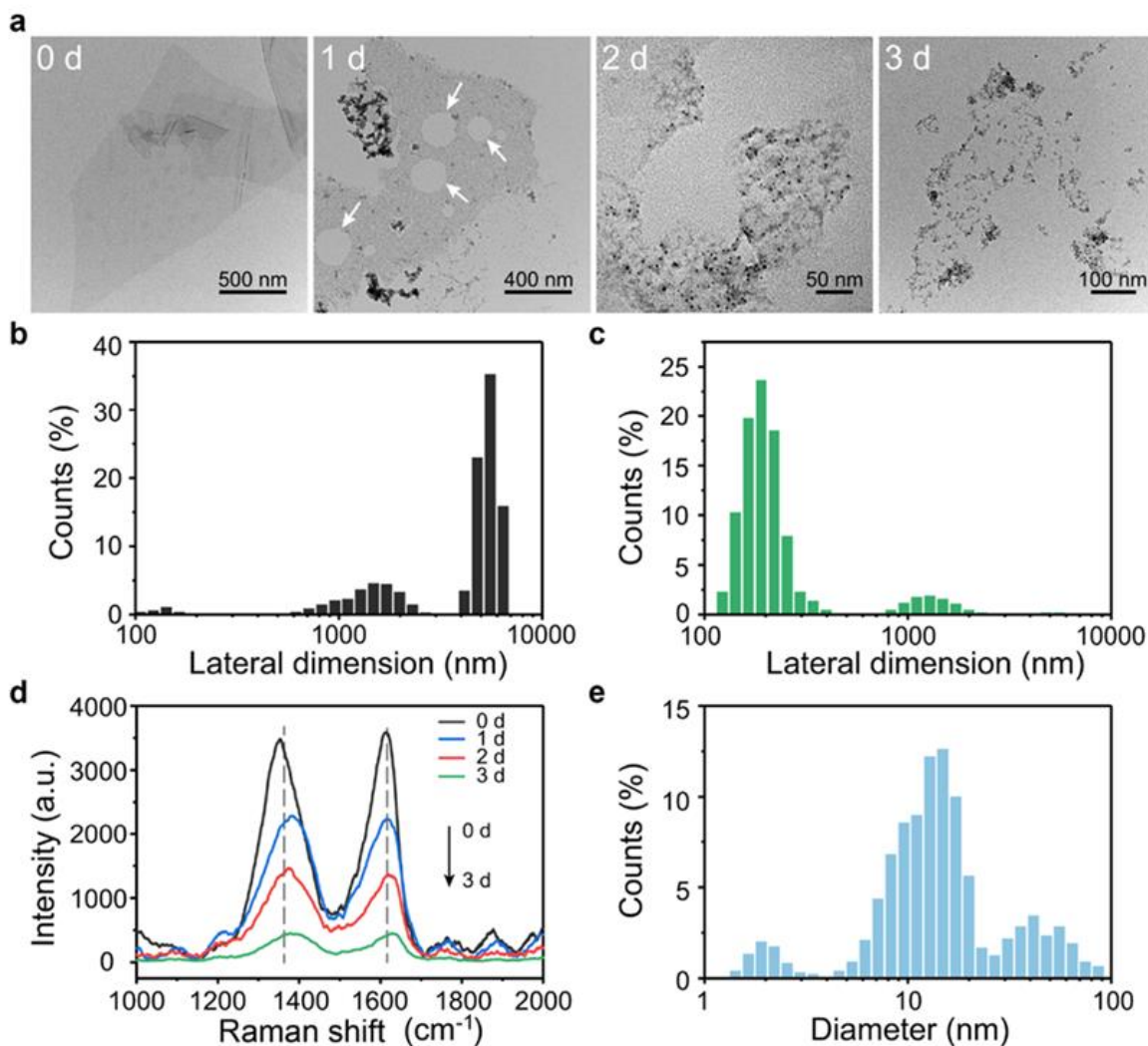


Fig. 1: GO is defensively degraded by neutrophils. a) TEM images of GO treated with neutrophils after 0, 1, 2, and 3 d. White arrows mark holes on GO sheets. Black dots were proteins secreted by neutrophils that adsorbed on the GO sheets. **b-c)** Histograms of GO lateral dimension distribution on 0 d (b) and 3 d (c) degraded by neutrophils, measured from TEM images. **d)** Raman spectra of GO sheets after 0, 1, 2, and 3 d biodegradation by neutrophils. D (1380 cm^{-1}) and G (1620 cm^{-1}) bands are plotted by dotted lines. **e)** Histograms of hole diameter distribution on 3 d, measured from TEM images. 0 ~ 3 d indicate 0 ~ 3 days after biodegradation.

Initially, we observed that both mGO and nGO were gradually degraded by neutrophils. TEM images showed that the characteristic sheet shape disappeared but visible “holes” formed on mGO sheets after 1 day (Fig. 1a). Besides, some proteins of neutrophils were adsorbed on GO sheets. When incubation extending to 2 days, considerable damaged parts on the basal plane of GO were visible. Eventually, residual mGO extensively degraded into nanometer-sized fragments after 3 days. The patterns of GO on 0 d (Fig. 1b) and 3 d (Fig. 1c) also indicated that GO were degraded from micrometer-size to nanometer-size. The morphology changes were also observed on nGO (Supplementary Fig. 3A). Moreover, crystalline phase changes of GO were also characterized by Raman spectroscopy (Fig. 1d; Supplementary Fig. 3B). Significant loss of disorder-induced D band (1380 cm^{-1}) and crystalline G band (1620 cm^{-1}) was

observed, indicating neutrophils destroyed the order degree of GO. We also measured the diameter of holes on mGO sheets after 3 days (Fig. 1e), and the average diameter of holes was 18.4 nm.

2.2. Distinct defensive behaviors of neutrophils depend on GO lateral dimension

Subsequently, we carefully explored the detailed biological changes of neutrophils during biodegradation by fluorescence imaging, scanning electron microscope (SEM), reactive oxygen species (ROS) detection and immunoblotting. As shown in Fig. 2a & b, for untreated control group, MPO and NE localized together in cytoplasm of neutrophils. For mGO groups, MPO and NE translocated to nucleus. Simultaneously, the nucleus disassembled and the web-like NETs were released as cell membrane broke. Moreover, neutrophils became flat and adhered to the substratum (Supplementary Fig. 4), suggesting that neutrophils underwent NETosis in line with previous study.^{16, 19} Therefore, mGO not only triggered the NETs formation but also appeared to be encased in web-like structures. By contrast, neutrophils secreted MPO after stimulating by nGO. NETs formation was not observed by immunofluorescence or SEM images. This indicated that neutrophils mainly secreted MPO to resist exogenous nGO by degranulation.²⁴

Moreover, the most distinct morphological changes of neutrophils were perimeter and shape in the nuclear area.²⁵ Thus, we defined four morphologies of nuclear as shown in Figure 2c: i) lobulated, ii) delobulated, iii) diffused, and iv) extended nuclei. Most neutrophils lost the typical lobulated nuclear due to undergoing NETosis or degranulation. Besides, 69.8% and 83.6% of neutrophils keep cell viability after treating with mGO or nGO (Fig. 2c), demonstrating that GO triggered a size-dependent loss of neutrophils viability. Taken together, the mechanism of neutrophils defense was lateral dimension dependent, namely, neutrophils released NETs upon stimulated with mGO, while neutrophils induced degranulation in response to nGO.

Mitochondrial ROS and the MPO-NE pathway are parallel key signals in degranulation and NETosis.²⁶ We evaluated mitochondrial ROS production elicited by mGO and nGO since NETosis requires ROS (Fig. 2d).^{18, 26, 27} We used phorbol 12-myristate 13-acetate (PMA), a pharmacological agonist to induce ROS as a side-by-side comparison of mGO and nGO-induced pathways.²⁸ Our results showed both mGO and nGO elicited ROS burst within 30 minutes. Therefore, ROS are essential upstream effectors in biodegradation. However, the activation of neutrophils with mGO led to an abundant production of ROS, whereas nGO-treated neutrophils produce lower ROS than PMA group.

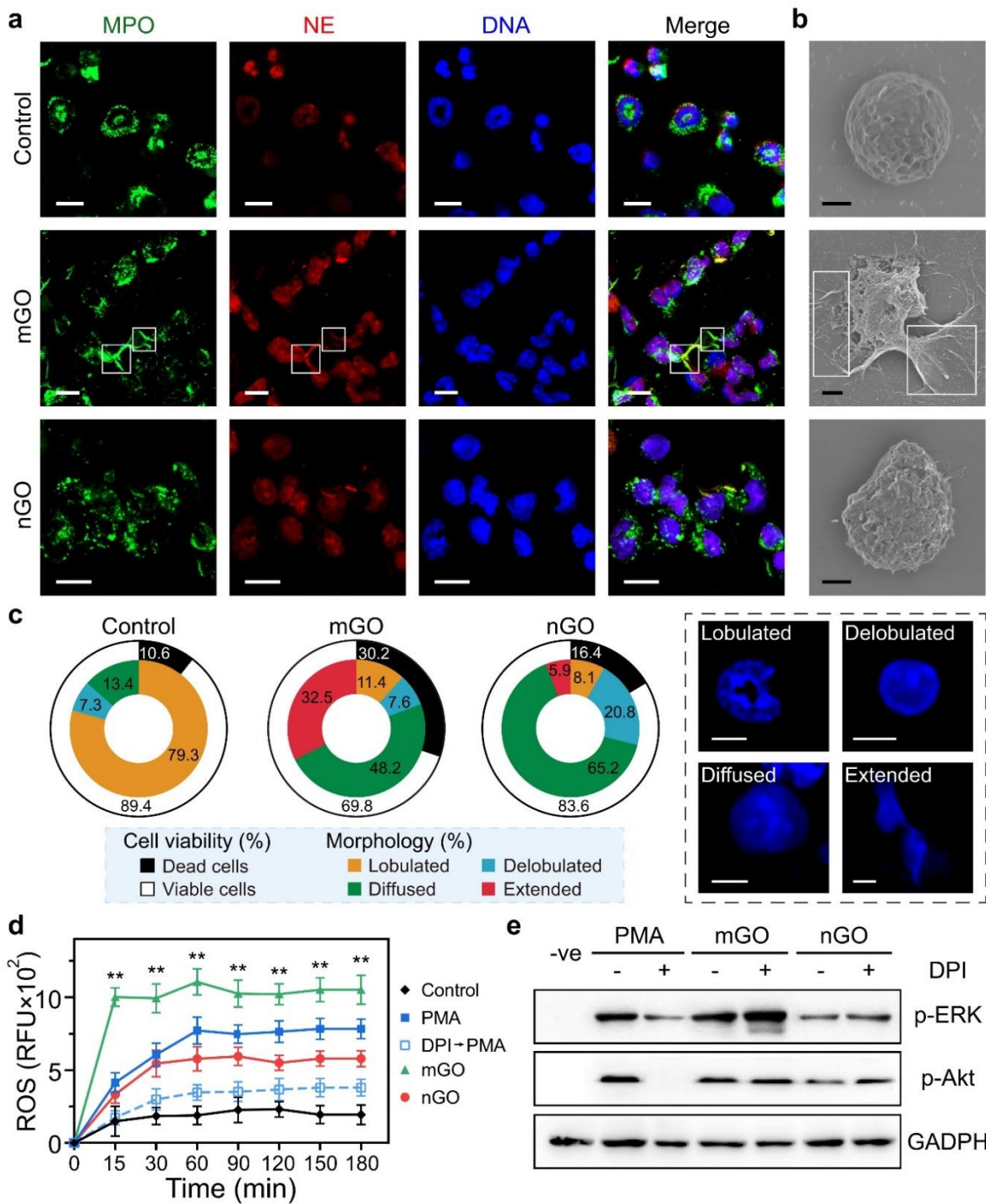


Fig. 2: Neutrophils defensively degrade GO in a lateral dimension dependent manner. **a)** Immunofluorescence confocal micrographs of localization of MPO (green), NE (red) and DAPI-stained DNA (blue) in mouse neutrophils incubated with media alone (top), mGO (medium) and nGO (bottom) after 2 h. Scale bars: 10 μm . **b)** SEM images of mouse neutrophils incubated with media alone (top), mGO (medium) and nGO (bottom) after 2 h. Scale bars: 2 μm . The release of NETs was indicated in white frames. **c)** Viability and nuclear morphologies of neutrophils with media alone (left), mGO (medium), and nGO (right) after 2 h. Four different morphologies are presented in dotted frame. Neutrophils viability were measured by quantification of cellular ATP. Scale bars: 5 μm . **d)** Mitochondrial ROS production in neutrophils stimulated with PMA, mGO, and nGO. Control, neutrophils incubated with media alone. DPI \rightarrow PMA, pretreated with DPI and activated with PMA. ****** $P < 0.01$ compared with control groups, two-way ANOVA. **e)** Immunoblot analysis of signaling kinases p-ERK and p-Akt. Higher expression of p-

ERK and p-Akt was observed in neutrophils stimulated by mGO than nGO. The activation of p-ERK in neutrophils stimulated with nGO were suppressed by DPI. –ve, negative control. GAPDH, glyceraldehyde-3-phosphate dehydrogenase were used as loading control. Data are representative of at least three independent experiments.

When neutrophils were pretreated with the NADPH oxidase (NOX) inhibitor diphenyleneiodonium (DPI),²⁹ ROS production in PMA-stimulated cells was significantly suppressed (Fig. 2d), resulted in inhibiting NETosis (Supplementary Fig. 5A). Hence, PMA-induced NETosis is NOX-dependent. Nevertheless, DPI didn't block NETs release in mGO groups, which indicated that mGO engaged NETs through a NOX-independent way (Supplementary Fig. 5B). Accordingly, mGO-induced NETosis is distinct from PMA-mediated NETosis. However, NE activity was blocked by DPI in nGO group, suggesting that neutrophils degranulation triggered by nGO was dependent on NOX (Supplementary Fig. 6).

We further explored the signaling pathway in the GO biodegradation. Since key kinases such as p-ERK²⁵ and p-Akt³⁰ have been shown involved in PMA-induced NETosis, we therefore assessed their differential activation by mGO or nGO. Our results showed that p-ERK and p-Akt were robustly activated by mGO. In contrast, nGO moderately activated p-ERK and p-Akt (Fig. 2e). The activation of p-ERK was 61.4% reduced in DPI-nGO-treated neutrophils (Supplementary Fig. 7). Although similar kinases were activated in mGO- and nGO-induced biodegradation, neutrophils switched to NETosis or degranulation resulting in different functional attributes to degrade GO in a lateral dimension dependent manner.

2.3. MPO is determinant mediator of GO biodegradation

Hydroxyl radical ($\cdot\text{OH}$) plays an important role in degrading carbon nanomaterials through reacting with double bonds ($\text{C}=\text{C}$).^{20, 31} Besides, it also oxidizes carbon nanomaterials to generate carboxyl and hydroxyl groups on surface.²¹ To confirm the high redox ability of hydroxyl radical, we firstly investigated MPO/H₂O₂/Cl⁻ system. Samples of GO/H₂O₂/Cl⁻ and GO/MPO/Cl⁻ were characterized by Raman spectra (Supplementary Fig. 8A, B). No biodegradation was observed in these samples, indicating that hypochlorous acid was a major oxidant in the reaction. Additionally, the biodegradation of GO was interrupted by MPO inhibitor, demonstrating such biodegradation was a MPO-mediated manner (Supplementary Fig. 8C).

Next, we focused on verifying MPO-mediated biodegradation of GO since the defensive effect of NETs is dependent on its major component of MPO with high redox ability.³² GO sheets were incubated with MPO at 37 °C in sterilized water containing sodium chloride (NaCl) with or without H₂O₂. The suspension was collected for subsequent analyses at 0, 12, and 24 h. Biodegradation was monitored by observing color change of reaction solution. After 24 h, the suspension became translucent (Supplementary Fig. 9).

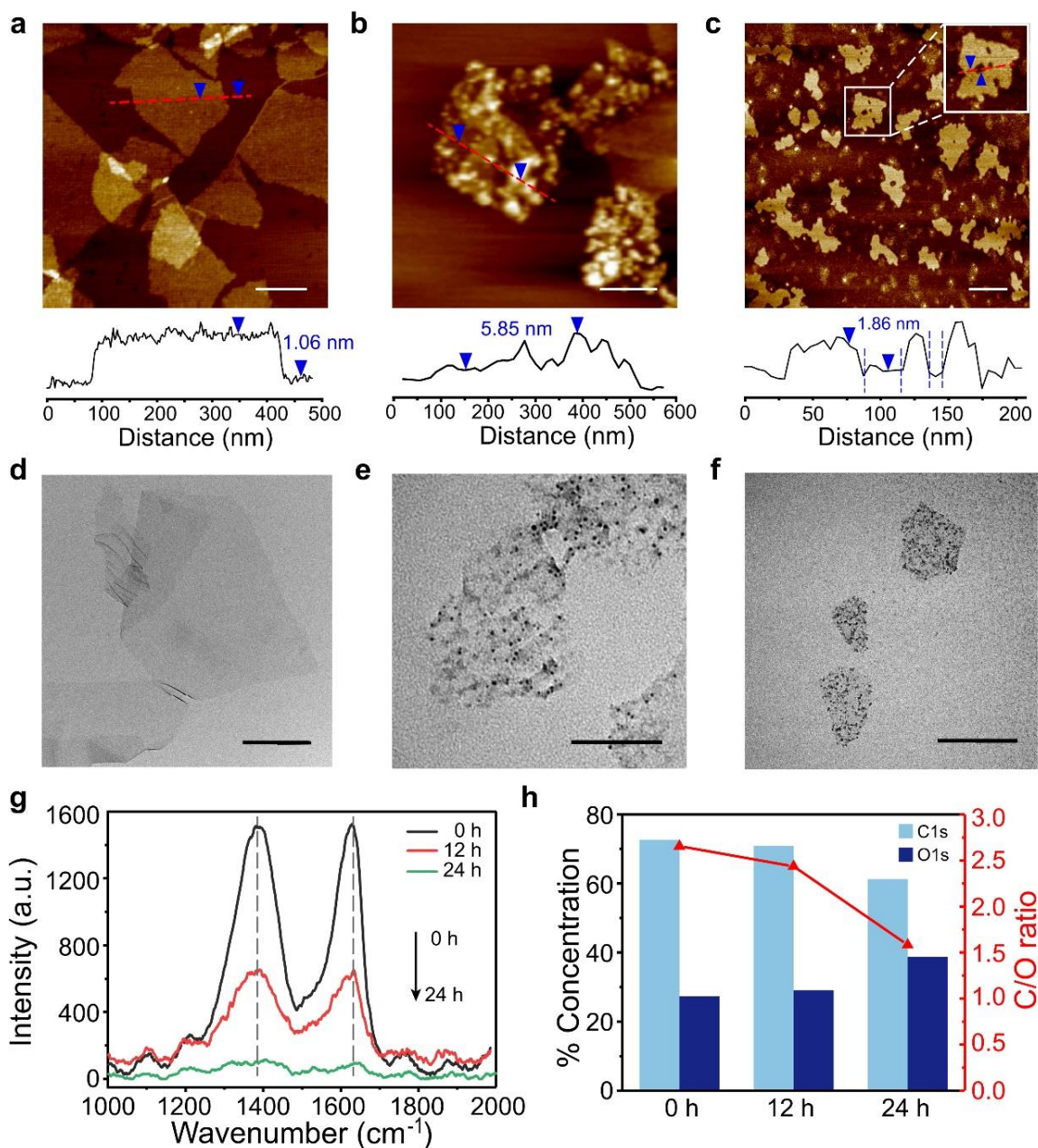


Fig. 3: Biodegradation of GO by MPO. a-f) AFM and TEM images of GO sheets before (a, d) and after incubating with recombinant mouse MPO in the presence of NaCl and H₂O₂ for 12 h (b, e), and 24 h (c, f), respectively. The black dots of TEM images were MPO adsorbed on GO sheets. The thickness analysis from the cross section is shown under corresponding images. Insert is the blow-up of the GO fragment with holes. All AFM images were acquired under the tapping mode. Scale bars: 200 nm. g) Raman spectra of GO sheets after 0, 12, and 24 h degradation. D (1380 cm⁻¹) and G (1620 cm⁻¹) bands are plotted by dotted lines. h) Concentration of C 1s and O 1s from XPS spectrum and the correlative C/O ratio at 0, 12 and 24 h.

To approve the MPO-mediated biodegradation of GO, we employed AFM and TEM to acquire the topography and thickness of GO sheets. As MPO is a highly cationic protein which tends to be attached on negatively charged surfaces like GO sheets, MPO was adsorbed on GO sheets during incubation. Initially, the monolayer GO sheets showed characteristic thickness of 1.06 nm (Fig. 3a). As adsorption of

MPO, the thickness of GO increased to 5.85 nm (12 h) and 1.86 nm (24 h), respectively (Fig. 3b, c). With expansion of hole areas in biodegradation, the sharp edge of GO became irregular and a large number of GO fragments were observed (Fig. 3d, e). After 24 h, the GO sheets were degraded into debris with lateral dimensions ranging from 20 to 100 nm (Fig. 3f).

Furthermore, Raman spectra characterized the crystalline phase changes of GO sheets (Fig. 3g). After 12 h, both D and G bands observably reduced with I_D/I_G decreasing from 1.03 to 1.01, indicating the GO sheets were partially degraded with little increase of defect density. After 24 h, both bands notably diminished, suggesting the GO sheets were degraded completely.

To examine the chemical composition variation of GO during the biodegradation, XPS spectra were acquired (Supplementary Fig. 10). Peaks at 284.8, 286.9, 287.9, and 288.8 eV corresponded to C-C in aromatic rings, C-O (epoxy and alkoxy), C=O (carbonyl), and C=O(OH) (carboxylic) groups individually.³¹ With the reaction proceeding, the intensity of C-O groups decreased dramatically, while the intensity of C=O and C=O(OH) groups increased gradually. As a result, the C/O atomic ratios were 2.66, 2.43 and 1.58 at 0, 12 and 24 h, respectively (Fig. 3h). Our data showed that the C-C and C-O bonds of GO in degradation were broken. Meanwhile, more periphery carbons were oxidized into the C=O or C=O(OH) groups.

2.4. Thermodynamics in MPO-mediated biodegradation

In this section, we investigated the thermodynamics of MPO-mediated biodegradation by intrinsic fluorescence measurement and molecular docking simulation. The thermodynamic parameters enthalpy change (ΔH^0) and entropy change (ΔS^0) were calculated according to the following van't Hoff equation³³

$$\ln K_a = -\frac{\Delta H^0}{RT} + \frac{\Delta S^0}{R} \quad (1)$$

where K_a refers to the binding constant, ΔG^0 is the free energy change, R is the gas constant, and T is absolute temperature. Since GO is a sensitive fluorescence quencher and is capable to quench spontaneous fluorescence of proteins molecules,³⁴ spectral measurements were used to obtain K_a .

Next, we calculated the fluorescence quenching parameters according to the modified Stern-Volmer equation³⁵

$$\frac{F_0}{\Delta F} = \frac{F_0}{F_0 - F} = \frac{1}{f_a K_{SV} [Q]} + \frac{1}{f_a} \quad (2)$$

where F_0 and F are the fluorescence intensities in the absence and presence of GO respectively, $[Q]$ is concentration of GO, K_{SV} is Stern–Volmer quenching constant of MPO by GO, and f_a is the fraction of accessible fluorescence.

Table 1. Thermodynamic parameters and binding constant in biodegradation at T₁ (298.15 K) and T₂ (310.15 K).

Temperature	K_{SV} ($\times 10^3 \text{ M}^{-1}$)	f_a	n	K_a ($\times 10^3 \text{ M}^{-1}$)	ΔG^0 ($\text{kJ}\cdot\text{mol}^{-1}$)	ΔH^0 ($\text{kJ}\cdot\text{mol}^{-1}$)	ΔS^0 ($\text{J}\cdot\text{mol}^{-1}\cdot\text{K}^{-1}$)
T ₁	40.46	1.23	1.1	46.77	-26.65	-5.9	69.6
T ₂	40.23	1.61	1.4	42.66	-27.49		

Our results showed that the intrinsic fluorescence intensity of MPO had a negative relationship with the concentration of GO at 298.15 K (T₁) and 310.15 K (T₂) (Fig. 4a; Supplementary Fig. 11). And there was a positive linear correlation between $F_0/\Delta F$ ratio and $\frac{1}{[Q]}$ (Fig. 4b). Hence, the values of K_{SV} were calculated according to equation (2) using values of F_0 and F from fluorescence measurements and the ordinate $\frac{1}{f_a}$ (Table 1; Fig. 4b). In addition, the values of K_{SV} decreased with temperature increasing, suggesting that the interaction of GO and MPO followed static quenching model.³⁶

To obtain the binding constant of K_a , we used equation (2) to

$$\log \left[\frac{F_0 - F}{F} \right] = \log K_a + n \log [Q] \quad (3)$$

where n is the binding number. Accordingly, the values of n and K_a were acquired from the slope and intercept of fitting curves, respectively (Fig. 4c; Table 1). The thermodynamic parameters of ΔG^0 , ΔH^0 and ΔS^0 are the main evidence for interaction forces, which could be estimated from the Gibbs equation³⁶

$$\Delta G^0 = \Delta H^0 - T\Delta S^0 = -RT \ln K_a \quad (4)$$

The calculated values of ΔG^0 , ΔH^0 and ΔS^0 at T₁ and T₂ were summarized in Table 1. The binding process of MPO and GO was spontaneous because of negative ΔG^0 . Furthermore, the negative ΔH^0 and positive ΔS^0 values indicated that electrostatic interactions were major causes during the binding process.

Subsequently, we calculated the distance between MPO and GO based on the above experimental FRET data. A transfer of energy could take place through direct electrodynamic interaction, which will happen under the condition that fluorescence emission spectrum of the donor (MPO) and UV-vis absorbance spectrum of the acceptor (GO) have overlap.^{36, 37} Figure 4d showed that the overlapping of emission spectrum of MPO and the absorption spectrum of GO, indicating the FRET occurred.

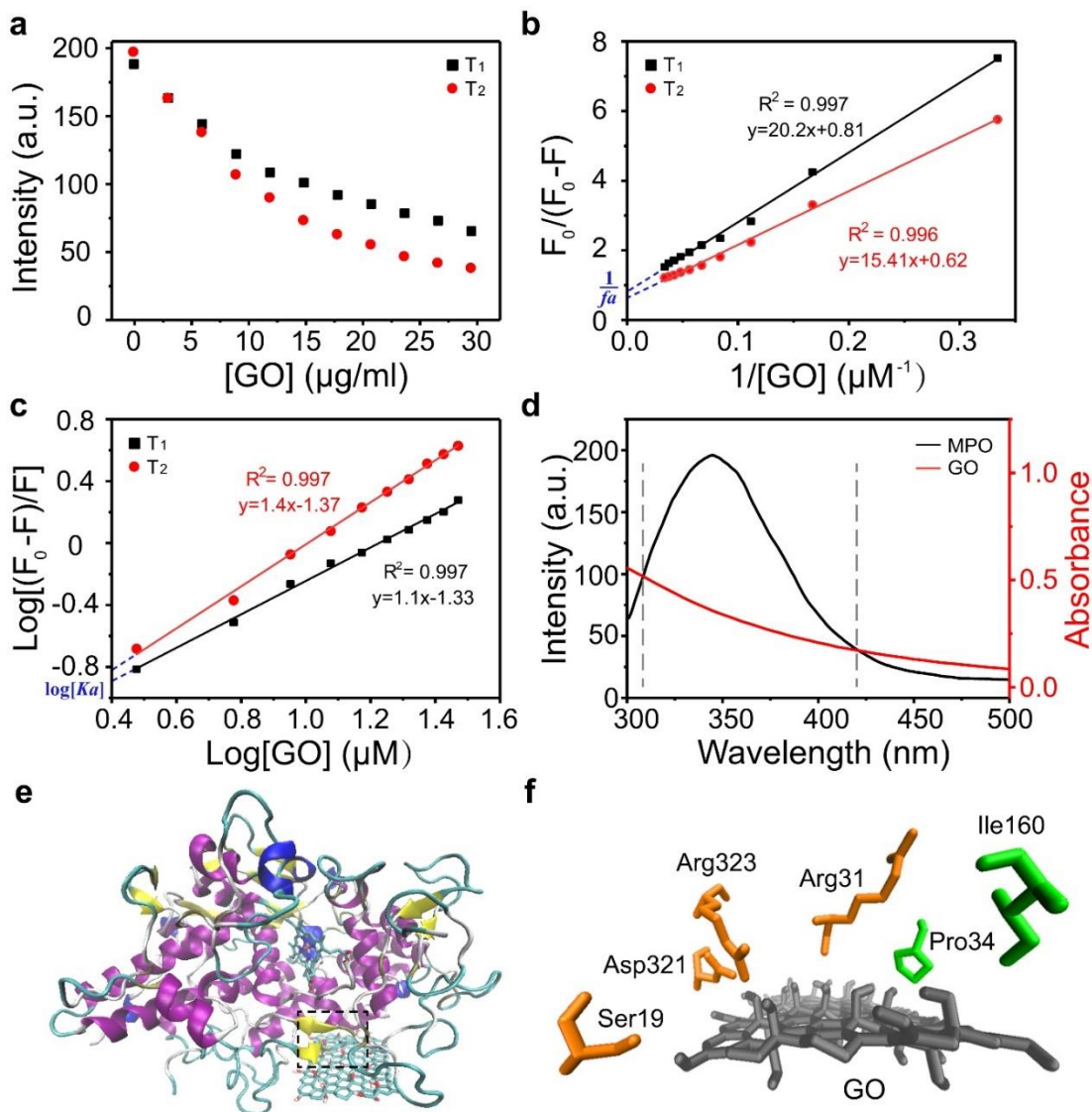


Fig. 4: Thermodynamics in MPO-mediated biodegradation. **a)** Changes in the maximum fluorescence emission of MPO with different concentrations of GO at temperature T_1 (black) and T_2 (red). **b)** Modified Stern-Volmer plots for the quenching constant (K_{SV}) in biodegradation at temperature T_1 (black) and T_2 (red). Data points are calculated using equation (2). **c)** Double log plot for the binding constant (K_a) and the number of binding sites (n) of MPO at T_1 (black) and T_2 (red), according to equation (3). **d)** Overlap of the fluorescence emission spectrum of MPO ($30 \mu\text{g mL}^{-1}$, black) and the absorbance spectrum of GO ($30 \mu\text{g mL}^{-1}$, red), which indicated within the range of two grey dashed lines. **e)** Binding site of MPO on GO predicted by molecular docking studies (AutoDock Vina). The binding site was indicated in dotted frame. **f)** The predicting residues of MPO participating in the biodegradation. T_1 equals 298.15 K and T_2 equals 310.15 K.

According to Förster theory of non-radioactive energy transfer,^{38, 39} we calculated that the Förster distance (R_0) was 2.4 nm and the spatial distance (r) between MPO and GO was 2.8 nm, which indicated that energy transfer from MPO to GO occurred with high probability.

To identify the binding manner, we performed molecular docking simulation using AutoDock Vina, a software to predict bound conformations and free energies of binding.⁴⁰ Our results showed that MPO had a single binding site with GO, consisting of Asp321, Arg323, Ser19, Arg31, Ile160 and Pro34 (Fig. 4e, f).

Specifically, Asp321, Arg323, Ser19, and Arg31 bound to GO through electrostatic interaction, while Ile160 and Pro34 relied on hydrophobic interaction. Comparatively, the binding manner between MPO and GO was inclined to electrostatic interaction. The calculated closet distance from GO to the binding site of MPO was 9.2 Å, and the binding energy was -69.8728 kJ·mol⁻¹.

2.5. Identify active sites on GO

We next investigated the active sites on basal plane or edge of GO. The heterogeneous electron-transfer (HET) rate was measured by two redox probes, namely potassium ferricyanide (K₃Fe(CN)₆) and hexaammineruthenium chloride (Ru(NH₃)₆Cl₃) as inner- and outer-sphere probes, respectively.⁴¹ The electrochemical signal of inner-sphere probe reflects the amount of electrochemically active sites and defects on the edges and basal plane of GO, which is also sensitive to oxygen functionalities.⁴² For outer-sphere probe, its electrochemical signal is influenced only by the amount of electrochemically active sites.⁴³

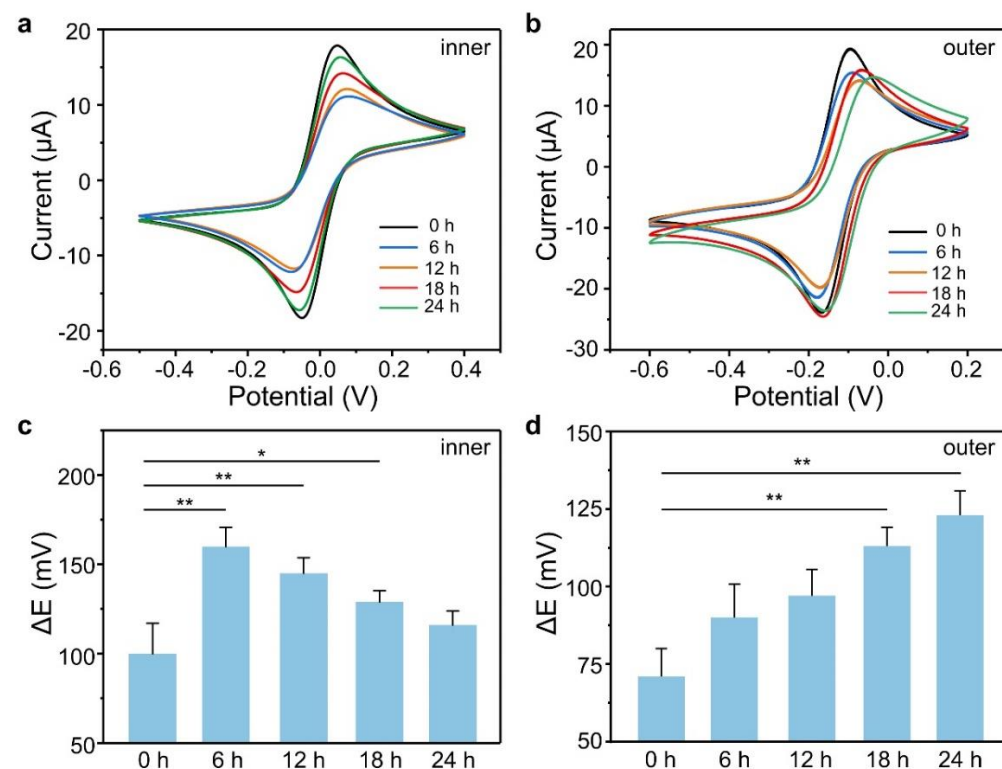


Fig. 5: Electrochemical behavior at basal and edge of GO during the biodegradation. A pair of redox probes: **a)** inner-sphere [Fe(CN)₆]^{3-/4-} and **b)** outer-sphere [Ru(NH₃)₆]^{2+/3+} probes are used to measure HET rate. Corresponding peak-to-peak separation values (ΔE) are calculated in **(c)** and **(d)**, respectively. HET rate is measured with 5mM redox probe in 100 mM KCl supporting electrolyte. Data are presented as mean ± SD. **P*<0.05, ***P*<0.01, compared with data of 0 h, one-way ANOVA.

The cyclic voltammograms (CVs) were firstly performed in basic reaction medium (phosphate buffer saline, PBS) to verify no presence of unrequired side reactions (Supplementary Fig. 12). According to the

CVs shown in Fig. 5a and 5b, the peak-to-peak separation values (ΔE) between control (0 h) and degraded samples were calculated respectively (Fig. 5c, d). For inner-sphere probe, the decreased ΔE values suggested more oxygen functionalities were introduced into GO with prolonged reaction time. The gap of ΔE values between 0 h and 6 h attributed to increase holes on the basal plane of GO and newly generated GO fragments. For outer-sphere probe, the ΔE values gradually rose up, which indicated more electrochemically active sites emerged on the edges of GO.

2.6. Mass spectrometry analysis of biodegradation products of GO

To explore the biodegradation products, samples of 0 d (as control) and 3 d were analyzed by matrix-assisted laser desorption-ionization time-of-flight mass spectrometry (MALDI-TOF MS). The mass spectra of GO biodegradation products ($[M-H]^-$ in negative ion mode) ranged from 300 to 500 Da ($\sim C_{25}$ to C_{40}) were shown in Fig. 6a & b. By day 3, more peaks presented in m/z 300 to 500, suggesting more chemical molecules formed during biodegradation reaction. Namely, in comparison with the mass spectra of GO on 0 d, the originally primary peak at m/z 327.0548 and 355.0706 disappeared while some new peaks of m/z 339.3282, 465.1836, 471.2374 and 483.2014 appeared on 3 d, indicating the large GO sheets had been cracked into smaller molecules.

To decipher the possible chemical composition and structures, major MS peaks detected in 3 d GO samples were putatively identified by accurate mass matching against the PubChem database (<https://pubchem.ncbi.nlm.nih.gov>). Our results indicated several structures containing benzotropolone nucleus with a *vic*-trihydroxyphenyl moiety or an *ortho*-dihydroxyphenyl (Fig. 6c). These potential molecular structures were very similar to catechin, epigallocatechin, epicatechin gallate and eucalyptin. This is consistent with our previous study that the debris of GO probably contained a lot of similar small molecules like flavonoids and polyphenols.⁶

Furthermore, we incubated freshly isolated neutrophils with biodegraded suspension of GO to evaluate the effects of such smaller molecules on neutrophils viability. In comparison with normal control (RPMI 1640 culture media) and positive control (PMA, a NETosis agonist), the biodegradation products containing smaller flavonoids-like molecules did not display any significant side-effect (Fig. 6d).

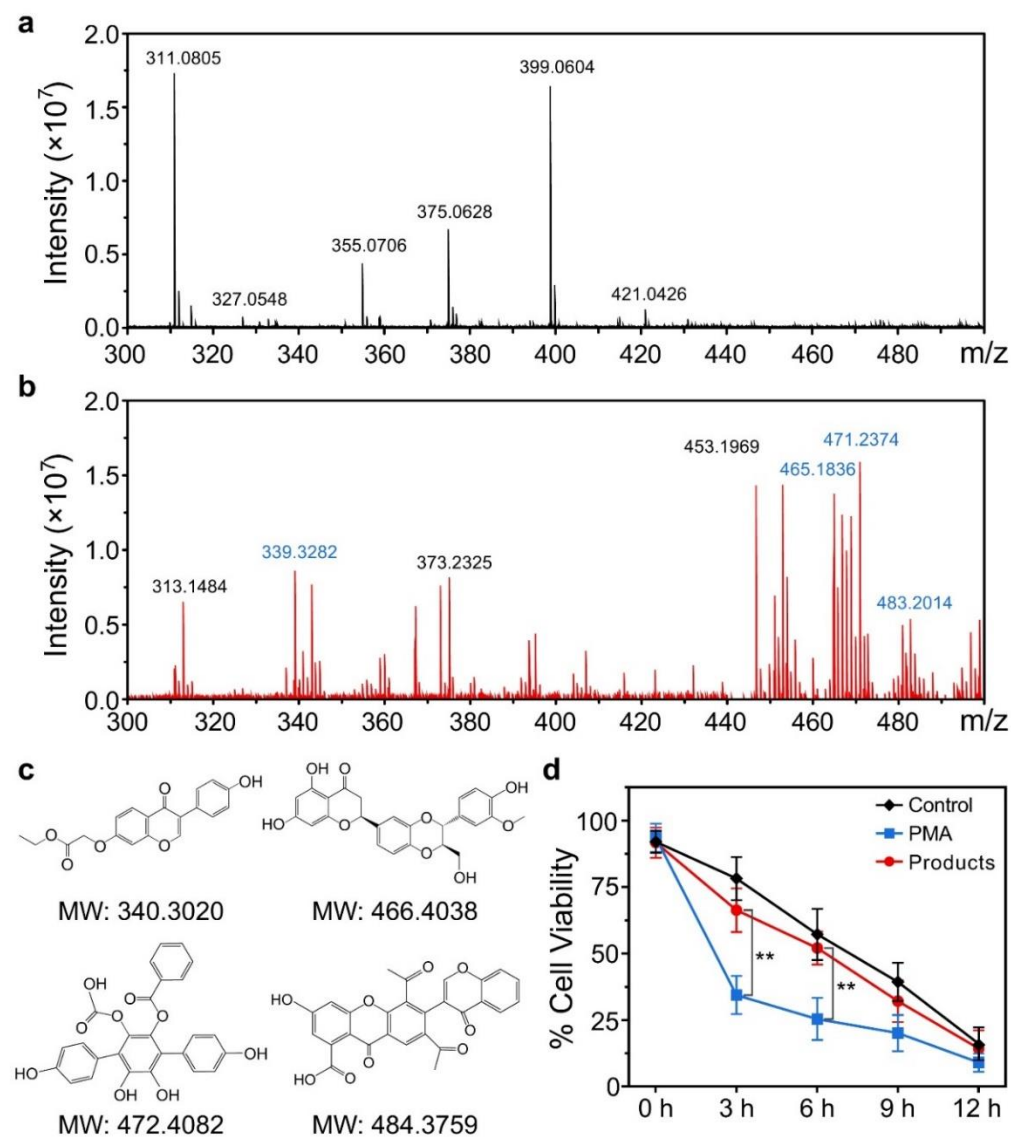


Fig. 6: Mass spectrometry analysis of biodegradation products of GO. MALDI-TOF MS spectra of GO biodegradation products by neutrophils on 0 d (a) and 3 d (b) ranged from m/z 300 to 500 (negative ion mode). c) Four major putative molecules from biodegradation products of GO were identified by MALDI-TOF MS. d) Neutrophils viability were determined by quantification of cellular ATP. Neutrophils were stimulated by biodegradation products, PMA or media alone. PMA is positive control. All data are presented as mean \pm SD. ** $P < 0.01$ compared with PMA, two-way ANOVA.

Based on the aforementioned thermodynamic analysis, electrochemical and mass spectrometry results, we speculated that biodegradation initiated at the carbon atoms connected with hydroxyl and epoxide groups (Fig. 7). A large amount of hydroxyl radical and peroxide radical was generated and attacked the carbon atoms in the presence of MPO/H₂O₂. Moreover, hydroxyl radicals would further oxidize GO through not only the conversion of oxygen moieties to higher oxidation states but also electrophilic addition to unsaturated bonds.⁴⁴ Interestingly, the newly formed oxygen-containing groups including the quinone group or radicals may serve as new oxidation reaction sites. As a result, the GO sheets were “cracked” into fragments, GO quantum dots, or even small molecules.

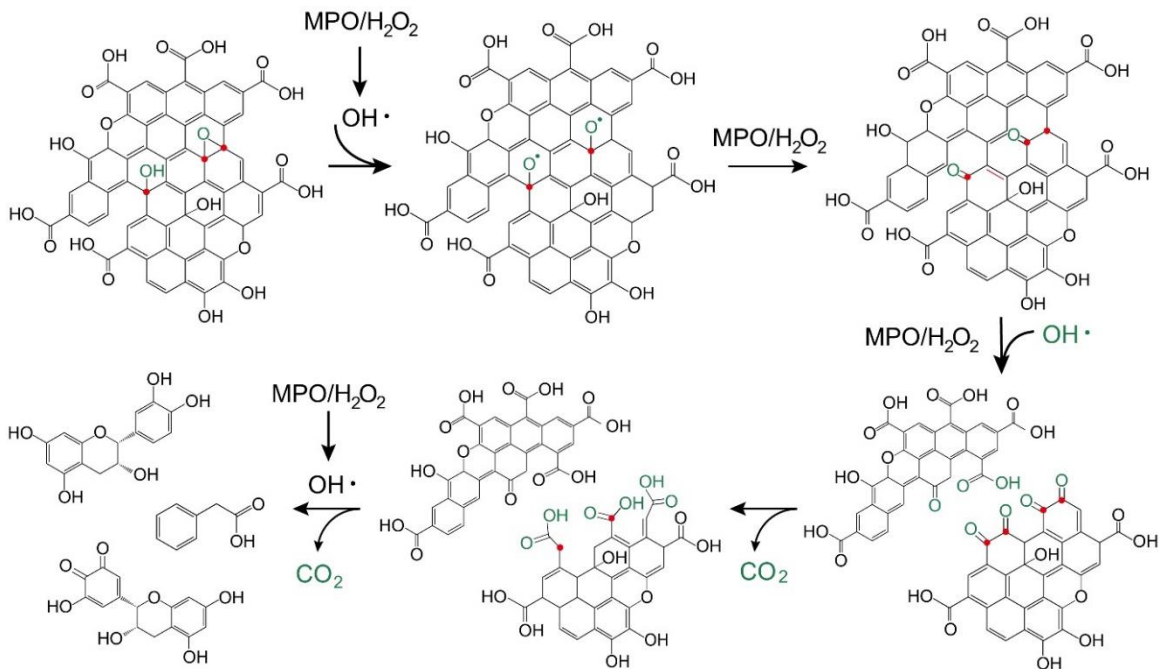


Fig. 7: Schematic of a proposed fragmentation pattern of MPO-mediated biodegradation of the GO sheets.

3. Conclusion

Understanding the interaction between GO and immune system is the key to implement GO from bench to bedside. In this work, we firstly discover that neutrophils spontaneously sense lateral dimension of GO, then degrade GO *via* NETs formation or degranulation. The lateral dimension of GO is a critical factor that regulates the “decision” of neutrophils. Once GO invades the organism, the neutrophils are recruited and become activated. Neutrophils release NETs in response to mGO through NOX-dependent pathway, or induce degranulation in response to nGO. The biodegradation is substantially MPO-catalyzed oxidation reaction. MPO consumes H₂O₂ to generate HOCl at the active sites where abundant oxygen functional groups and defects present. Furthermore, our data have demonstrated the biodegradation products of GO are flavonoids and polyphenols such as catechin, epigallocatechin and eucalyptin, which usually are abundant in plants and nutritional supplements without potential risk to immune system.^{45, 46, 47}

Intriguingly, larger-sized invaders are more effective at inducing NETosis, suggesting that NETs enhance effective immune defense and promote synergy between MPO and other various antimicrobials to minimize spread of invaders.³² Since NETs release the same antimicrobials including MPO as degranulation, we are curious about why neutrophils undergo NET formation at the cost of “suicide” other than the release of histones. Due to immune-modulatory properties of neutrophils, advantages of NETs are rational. First, NETs minimize destruction to surrounding tissues and coordinate the inflammatory response. Secondly, neutrophils only pay the cost of shedding NETs like a scaffold, instead of high cellular energy for chemotaxis and uptake of invaders.³² Thirdly, the average life span of NETs is more than 24

h,⁴⁸ which persists much longer than phagocytosis or degranulation. Finally, given the web-like structure of NETs, they serve as physical carriers which prevent invaders from escaping. Collectively, neutrophils selectively switch defense strategies to achieve efficient goals (GO biodegradation) with minimum cost. The decision is simple but smart as the host defense of innate immune system.

Sustainable nanotechnology requires a comprehensive and scientific risk evaluation including exposure pathways and fate of nanomaterials.^{49, 50} Previous work have reported the *in vivo* toxicity of GO such as acute injures to lung and liver.^{51, 52} Moreover, carbon nanotubes became the first nanomaterial to be added to the SIN ('Substitute It Now') List by the Swedish non-profit organization in recent years, which aroused the attention on the future of sustainable nanotechnology.⁵³ Our study of the interaction between immune system and nanomaterials elucidated the immune effect on human health and environment. Our research provides fundamental guidance and experimental evidences for practical application of GO in sustainable nanotechnology, including but not limited to vaccine adjuvant development and drug carrier development.

4. Experimental Section/Methods

Synthesis, Modification and Characterization of GO: Both mGO and nGO were synthesized using the modified Hummers' method as our previous study described⁶. The characterization of GO sheets was performed by optical microscope (BX53M, Olympus, Japan), atomic force microscope (AFM) (Multimode 8, Bruker, Germany), transmission electron microscopy (TEM) (Talos L120C, Thermo Scientific, USA), X-ray photoelectron spectroscopy (XPS) (AXIS ultraDLD, Kratos, Japan), Raman spectroscopy (Finder Vista, Zolix, China), and Zeta potential (Zetasizer Nano ZSP, Malvern Panalytical, UK).

Optical microscopy: Samples (mGO) were prepared on a glass slide by depositing 20 μL of GO dispersed in Milli-Q water (Merck Millipore, UK) to a final concentration of 20 $\mu\text{g}\cdot\text{mL}^{-1}$. Samples were observed using a microscope (BX53M, Olympus, Japan) in bright-field at a magnification of 100 \times after drying in ambient for 2 h at room temperature. GO sheets were manually measured on ImageJ (version 1.44p, NIH, USA) by determining the longest Feret diameter in each object.

Atomic force microscopy: A Multimode 8 scanning probe microscope (Bruker, Germany) was utilized in tapping mode for height, sectional and phase analysis. Images were taken in air, using commercially available AFM cantilever tips with force constant of 42 $\text{N}\cdot\text{m}^{-1}$ and resonance vibration frequency of 350 kHz (Bruker, Germany). All samples for AFM analysis were prepared by drop-casting 10 μL sample on freshly cleaved mica sheet. Excess unbound materials were removed by washing with deionized water (Milli-Q, Millipore, USA) and then allowed to dry in ambient, which was repeated twice. AFM images were processed on Nanoscope Analysis software (version 1.5, Bruker, UK) for further statistical analysis.

Transmission Electron Microscopy: TEM was performed with a Talos L120C 120 kV electron

microscope (Thermo Scientific, USA). Samples were centrifuged at 3000 rpm for 15 min and decanted of supernatant to remove salt contributions. Then, the samples were resuspended into deionized water by sonication for 30 s (final concentration was $10 \mu\text{g}\cdot\text{mL}^{-1}$). $5 \mu\text{L}$ of each sample were deposited on a carbon coated copper grids and dried for 2 h prior to the TEM analysis. Lateral dimension distribution was manually measured on ImageJ software on several TEM images.

Raman Spectroscopy: All spectra were collected on a Raman microscope (Finder Vista, Zolix, China) at 533 nm laser excitation. Samples were scanned from 1000 to 2000 cm^{-1} to visualize the D and G bands, with a 15 s exposure time and averaged across 5 scans per location. Samples were prepared by dropping $20 \mu\text{L}$ aqueous suspension of samples on the surface of freshly cleaved mica and drying under ambient condition.

Neutrophil Isolation and Culture: Neutrophils were freshly isolated from mouse bone marrow and purified by magnetic active cell sorting (Miltenyi Biotec, Germany). After incubation with a cocktail of biotinylated antibodies and anti-biotin microbeads, non-neutrophils were depletion. Isolated neutrophils were maintained in phenol red-free RPMI-1640 culture medium (Gibco, USA) supplemented with 2 mM L-glutamine (Cyagen, USA), 100 U mL^{-1} penicillin (Cyagen, USA), and $100 \mu\text{g}\cdot\text{mL}^{-1}$ streptomycin (Cyagen, USA) without serum in 5% CO_2 incubator at $37 \text{ }^\circ\text{C}$.

Degradation by MPO and H_2O_2 : $10 \mu\text{g}$ lyophilized MPO (R&D Systems, USA) solubilized in $1\times\text{PBS}$ (final concentration of MPO: $10 \mu\text{g}\cdot\text{mL}^{-1}$) and $100 \mu\text{g}$ GO dispersed in autoclaved Milli-Q water (final concentration of GO: $100 \mu\text{g}\cdot\text{mL}^{-1}$) were mixed in a vial containing 140 mM NaCl (Sinopharm, China) and $100 \mu\text{M}$ diethylene triamine pentaacetic acid (DTPA, Sigma-Aldrich, USA) at a final volume of 1.0 mL. H_2O_2 ($100 \mu\text{M}$, Acros Organics, USA) was added every hour, and MPO was renewed every 6 h. All vials were then wrapped with parafilm and maintained at $37 \text{ }^\circ\text{C}$. The reaction was stopped by freezing the samples after 6, 12, 18, and 24 h of incubation time in $-20 \text{ }^\circ\text{C}$ refrigerator for further analyses. The control samples were performed using the sample protocol in the absence of H_2O_2 or MPO.

Confocal Microscopy: Mouse neutrophils at a density of 1×10^6 cells/mL were planted on poly-L-lysine coverslips in a 24-well plate, followed by incubation with media alone, mGO ($30 \mu\text{g}\cdot\text{mL}^{-1}$), and nGO ($30 \mu\text{g}\cdot\text{mL}^{-1}$) for 2 h at $37 \text{ }^\circ\text{C}$, in a humidified 5% CO_2 incubator. Next, cells were fixed in 2% paraformaldehyde for 20 min and blocked with 3% BSA in PBS solution for 30 min at room temperature. Staining with primary rabbit antibody against NE (Abcam, UK) and mouse antibody against MPO (FITC, Abcam, UK) at 1:200 in 1% BSA in PBS were performed for overnight at $4 \text{ }^\circ\text{C}$, followed by staining with secondary fluorescein Alexa Fluor 594 AffiniPure Goat anti-rabbit antibody (Yeasen Biotech, China) at 1:300 in 1% BSA in PBS for 1 h at room temperature. DAPI (Thermo Fisher, USA) was added for detection DNA. Slides were visualized with a confocal microscope (Zeiss LSM 880, Carl Zeiss, Germany).

Cell viability: Cell viability was measured by the quantification of cellular ATP. Neutrophils were freshly isolated and seeded at a density of 1×10^6 cells/mL in 96-well plates in phenol red-free RPMI-1640

cell medium. Then cells were incubated with PMA (Sigma-Aldrich, USA), biodegradation products or cell medium alone at 37 °C in a humidified 5% CO₂ incubator. Cells were lysed and measured using an ATP Assay Kit (Beyotime, China) according to the manufacturer's instructions. The relative light units were measured in a microplate reader (Synergy H1, BioTek, USA). The standard curve was used to calculate the ATP concentration.

Mitochondrial ROS detection: Mitochondrial ROS levels were measured in a microplate reader (Synergy H1, BioTek, USA). Cells were stained with 5 μM MitoSOX (Beyotime, China) at 37 °C for 30 min. After washing with PBS solution twice, cells in 24-well plate were incubated with PMA (25 nM), mGO (30 μg·mL⁻¹), and nGO (30 μg·mL⁻¹) in the absence or presence of DPI (10 μM) (MCE, USA). Then fluorescence distribution was detected at an excitation wavelength of 510 nm and at an emission wavelength of 580 nm.

Immunoblot: Cells after activation were lysed with a lysis buffer containing protease inhibitor mixture (Roche, Switzerland) and the supernatant was collected after centrifugation and homogenized by sonication. The protein concentration was measured using a BCA assay kit (Thermo Fisher, USA) as per instructions. The prepared lysates were thermally denatured in a 95 °C metal bath for 10 min. Then samples were electrophoretically separated *via* 10% SDS-PAGE before transferring to PVDF films (Millipore, USA). The PVDF films were then blocked with skim milk powder (Servicebio, China), incubated with primary antibody and HRP-secondary antibody and imaged with an imaging system (5200, Tanon, China). The antibodies of anti-phospho-ERK1/2 and anti-phospho-Akt (ABclonal, China) were used at 1:1000 dilutions.

X-ray photoelectron spectroscopy: XPS measurements were performed on an Axis UltraDLD spectrometer (Kratos, Japan) using a monochromated Al K α source at 15 kV. All binding energies at various peaks were calibrated using the binding energy of C1s (284.8 eV) according to NIST.

Zeta Potential: The surface charge of nGO and mGO was measured by Zetasizer Nano ZSP (Malvern Panalytical, UK) spectrometer in a disposable Zetasizer cuvettes (Malvern Panalytical, UK). Samples were sonicated for 5 min before the measurements. All values were converted automatically for triplicate measurements.

Fluorescence Spectroscopy: Fluorescence studies were carried out using a fluorescence spectrophotometer (Cary Eclipse, Agilent Technologies, USA) at an excitation wavelength of 280 nm. The emission spectra of all samples in the absence and presence of different concentrations of GO were recorded in the 300 to 500 nm range at ambient temperatures (298.15 and 310.15 K). The path length of the fluorescence cuvettes used for measurements was 0.7 cm. The excitation and emission slit widths were both set at 10 nm, respectively. The overlap of fluorescence emission spectrum of MPO and the UV-absorbance spectrum of GO was measured on UV-vis spectrometer (Cary 60, Agilent Technologies, USA), which were recorded in 300 to 500 nm.

Molecular Docking: To indicate GO interaction mode and binding parameters theoretically with MPO, the molecular docking calculations were performed using AutoDock Vina software.⁵⁴ GO molecular structures were modeled using the Hyperchem 8.0.6 program and VMD package.⁵⁵ Then, the geometry of them using the theoretical level of B3LYP with a 6-31G basis set that implemented in the Gaussian 98 program was optimized to minimize energy. MPO crystal structure (PDB ID: 1DNU) was used for the molecular docking calculations and obtained from the RCSB Protein Data Bank (<http://www.rcsb.org>). According to instruction, the PDBQT files of MPO and GO were prepared and then analyzed using the AutoDock Tools 1.5.4 package.⁵⁶

Electrochemical Detection: The electrochemical characterization by means of cyclic voltammetry was performed with a CHI 660E electrochemical workstation (CH Instruments, China) with gold microelectrodes fabricated as previously described.⁵⁷ The microelectrodes were placed into an electrochemical cell containing the electrolyte solution. PBS (100 mM, pH 7.4) was used as blank buffer and the supporting buffer for the redox probes. The aqueous solution containing 0.1 M potassium chloride (KCl) (Sangon, China), 5 mM of $K_3[Fe(CN)_6]$ or $Ru(NH_3)_6Cl_3$ (Adamas, China) were prepared for inner- and outer-sphere redox probes, respectively. The scan rate used for CV measurements was $0.1 V \cdot s^{-1}$.

MALDI-TOF MS: MALDI-TOF mass spectra were acquired on a SolariX 7.0T FT ICR MS (Bruker, Germany) equipped a liner TOF instrument. Lyophilized biodegradation samples at different time point were resuspended in Milli-Q water at a concentration of $100 \mu g \cdot mL^{-1}$. CHCA (α -cyano-4-hydroxycinnamic acid, Sigma-Aldrich, USA) was used as the MALDI matrix. 5 μL of the sample matrix mixture was spotted on a gold array MALDI plate (Bruker, Germany) and dried under ambient conditions. Nitrogen laser was used for ionization at the negative ion mode for GO samples.

Statistical Analysis: All data are presented as mean \pm SD. Statistical analysis was performed using GraphPad Prism statistical analysis software (Version 8.0). Comparisons between different groups were performed using student's *t* test. A level of $P < 0.05$ was regarded as a significant.

Acknowledgements

This work was supported by Nature Scientific Foundation of China (Nos. 81871448, 81971736 and 81921002), National Key Research and Development Program of China (No. 2017FYA0205301), Shanghai Municipal Science and Technology (Nos. 2017SHZDZX01, 17DZ2203400 and 18430760500), Training Foundation for Young Talents of Shanghai Jiao Tong University (No. 18X100040040), and the Medical-Engineering Cross Foundation of Shanghai Jiao Tong University (Nos. ZH2018QNA49, ZH2018QNA51 and YG2021QN58).

References

1. Kim, J. et al. Graphene oxide sheets at interfaces. *J. Am. Chem. Soc.*, **132**, 8180-8186 (2010).
2. Pei, S. F. et al. Green synthesis of graphene oxide by seconds timescale water electrolytic oxidation. *Nat. Commun.*, **9**, (2018).
3. Bonaccorso, F. et al. Graphene, related two-dimensional crystals, and hybrid systems for energy conversion and

- storage. *Science*, **347**, 10 (2015).
4. Weiss, C. et al. Toward nanotechnology-enabled approaches against the covid-19 pandemic. *ACS Nano*, **14**, 6383-6406 (2020).
 5. Yao, B. et al. Paper-based electrodes for flexible energy storage devices. *Advanced Science*, **4**, 32 (2017).
 6. Meng, C. C. et al. Graphene oxides decorated with carnosine as an adjuvant to modulate innate immune and improve adaptive immunity in vivo. *ACS Nano*, **10**, 2203-2213 (2016).
 7. Yu, Z. et al. Boosting polysulfide redox kinetics by graphene-supported ni nanoparticles with carbon coating. *Adv. Energy Mater.*, **10**, 9 (2020).
 8. Seo, D. H. et al. Anti-fouling graphene-based membranes for effective water desalination. *Nat. Commun.*, **9**, 12 (2018).
 9. Svendsen, C. et al. Key principles and operational practices for improved nanotechnology environmental exposure assessment. *Nat. Nanotechnol.*, 12 (2020).
 10. Kolaczowska, E. & Kubes, P. Neutrophil recruitment and function in health and inflammation. *Nat. Rev. Immunol.*, **13**, 159-175 (2013).
 11. Mukherjee, S. P. et al. Graphene oxide elicits membrane lipid changes and neutrophil extracellular trap formation. *Chem*, **4**, 334-358 (2018).
 12. Han, J. et al. Dual roles of graphene oxide to attenuate inflammation and elicit timely polarization of macrophage phenotypes for cardiac repair. *ACS Nano*, **12**, 1959-1977 (2018).
 13. Li, Y. F. et al. Graphene microsheets enter cells through spontaneous membrane penetration at edge asperities and corner sites. *Proc. Natl. Acad. Sci. U. S. A.*, **110**, 12295-12300 (2013).
 14. Borregaard, N. Neutrophils, from marrow to microbes. *Immunity*, **33**, 657-670 (2010).
 15. Jorgensen, I. et al. Programmed cell death as a defence against infection. *Nat. Rev. Immunol.*, **17**, 151-164 (2017).
 16. Branzk, N. et al. Neutrophils sense microbe size and selectively release neutrophil extracellular traps in response to large pathogens. *Nat. Immunol.*, **15**, 1017-1025 (2014).
 17. Kenny, E. F. et al. Diverse stimuli engage different neutrophil extracellular trap pathways. *Elife*, **6**, 21 (2017).
 18. Metzler, K. D. et al. Myeloperoxidase is required for neutrophil extracellular trap formation: Implications for innate immunity. *Blood*, **117**, 953-959 (2011).
 19. Papayannopoulos, V. et al. Neutrophil elastase and myeloperoxidase regulate the formation of neutrophil extracellular traps. *J. Cell Biol.*, **191**, 677-691 (2010).
 20. Kagan, V. E. et al. Carbon nanotubes degraded by neutrophil myeloperoxidase induce less pulmonary inflammation. *Nat. Nanotechnol.*, **5**, 354-359 (2010).
 21. Kurapati, R. et al. Dispersibility-dependent biodegradation of graphene oxide by myeloperoxidase. *Small*, **11**, 3985-3994 (2015).
 22. Mukherjee, S. P. et al. Graphene oxide is degraded by neutrophils and the degradation products are non-genotoxic. *Nanoscale*, **10**, 1180-1188 (2018).
 23. Pillay, J. et al. In vivo labeling with ²H₂O reveals a human neutrophil lifespan of 5.4 days. *Blood*, **116**, 625-627 (2010).
 24. Lacy, P. Mechanisms of degranulation in neutrophils. *Allergy Asthma Clin. Immunol.*, **2**, 98-108 (2006).
 25. Hakkim, A. et al. Activation of the Raf-MEK-ERK pathway is required for neutrophil extracellular trap formation. *Nat. Chem. Biol.*, **7**, 75-77 (2011).
 26. Manfredi, A. A. et al. The neutrophil's choice: Phagocytose vs make neutrophil extracellular traps. *Front. Immunol.*, **9**, 13 (2018).
 27. Fuchs, T. A. et al. Novel cell death program leads to neutrophil extracellular traps. *J. Cell Biol.*, **176**, 231-241 (2007).
 28. Warnatsch, A. et al. Reactive oxygen species localization programs inflammation to clear microbes of different size. *Immunity*, **46**, 421-432 (2017).
 29. Douda, D. N. et al. SK3 channel and mitochondrial ros mediate nadph oxidase-independent netosis induced by calcium influx. *Proc. Natl. Acad. Sci. U. S. A.*, **112**, 2817-2822 (2015).
 30. Douda, D. N. et al. Akt is essential to induce nadph-dependent netosis and to switch the neutrophil death to apoptosis. *Blood*, **123**, 597-600 (2014).
 31. Zhou, X. J. et al. Photo-fenton reaction of graphene oxide: A new strategy to prepare graphene quantum dots for DNA cleavage. *ACS Nano*, **6**, 6592-6599 (2012).
 32. Papayannopoulos, V. & Zychlinsky, A. NETs: A new strategy for using old weapons. *Trends Immunol.*, **30**, 513-521 (2009).
 33. Ross, P. D. & Subramanian, S. Thermodynamics of protein association reactions: Forces contributing to stability. *Biochemistry*, **20**, 3096-3102 (1981).
 34. Kaminska, I. et al. Distance dependence of single-molecule energy transfer to graphene measured with DNA origami nanopositioners. *Nano Lett.*, **19**, 4257-4262 (2019).
 35. Sinkeldam, R. W. et al. Fluorescent analogs of biomolecular building blocks: Design, properties, and applications. *Chem. Rev.*, **110**, 2579-2619 (2010).
 36. Hu, Y. J. et al. Investigation of the interaction between berberine and human serum albumin. *Biomacromolecules*, **10**, 517-521 (2009).
 37. Forster & Frster, T. *Annalen der Physik (Leipzig)*, **437**, 55-75 (1948).
 38. Ghisaidoobe, A. B. T. & Chung, S. J. Intrinsic tryptophan fluorescence in the detection and analysis of proteins: A focus

- on forster resonance energy transfer techniques. *Int. J. Mol. Sci.*, **15**, 22518-22538 (2014).
39. van de Weert, M.&Stella, L. Fluorescence quenching and ligand binding: A critical discussion of a popular methodology. *J. Mol. Struct.*, **998**, 144-150 (2011).
40. Forli, S. et al. Computational protein-ligand docking and virtual drug screening with the autodock suite. *Nat. Protoc.*, **11**, 905-919 (2016).
41. Zhong, J. H. et al. Quantitative correlation between defect density and heterogeneous electron transfer rate of single layer graphene. *J. Am. Chem. Soc.*, **136**, 16609-16617 (2014).
42. Ji, X. B. et al. Oxygenated edge plane sites slow the electron transfer of the ferro-/ferricyanide redox couple at graphite electrodes. *Chemphyschem*, **7**, 1337-1344 (2006).
43. Mazanek, V. et al. Ultrapure graphene is a poor electrocatalyst: Definitive proof of the key role of metallic impurities in graphene-based electrocatalysis. *ACS Nano*, **13**, 1574-1582 (2019).
44. Bai, H. et al. Insight into the mechanism of graphene oxide degradation via the photo-fenton reaction. *J. Phys. Chem. C*, **118**, 10519-10529 (2014).
45. Cabrera, C. et al. Beneficial effects of green tea - a review. *J. Am. Coll. Nutr.*, **25**, 79-99 (2006).
46. Singh, B. N. et al. Green tea catechin, epigallocatechin-3-gallate (EGCG): Mechanisms, perspectives and clinical applications. *Biochem. Pharmacol.*, **82**, 1807-1821 (2011).
47. Kim, H. S. et al. New insights into the mechanisms of polyphenols beyond antioxidant properties; lessons from the green tea polyphenol, epigallocatechin 3-gallate. *Redox Biology*, **2**, 187-195 (2014).
48. Ley, K. et al. Neutrophils: New insights and open questions. *Science Immunology*, **3**, 14 (2018).
49. Svendsen, C. et al. Key principles and operational practices for improved nanotechnology environmental exposure assessment. *Nat. Nanotechnol.*, **15**, 731-742 (2020).
50. Lu, X. et al. Long-term pulmonary exposure to multi-walled carbon nanotubes promotes breast cancer metastatic cascades. *Nat. Nanotechnol.*, **14**, 719-727 (2019).
51. Rodrigues, A. F. et al. Size-dependent pulmonary impact of thin graphene oxide sheets in mice: Toward safe-by-design. *Advanced Science*, **7**, (2020).
52. Hu, H. et al. Gas identification with graphene plasmons. *Nat. Commun.*, **10**, (2019).
53. Hansen, S. F.&Lennquist, A. Carbon nanotubes added to the sin list as a nanomaterial of very high concern. *Nat. Nanotechnol.*, **15**, 3-4 (2020).
54. Trott, O.&Olson, A. J. Autodock vina: Improving the speed and accuracy of docking with a new scoring function, efficient optimization, and multithreading. *J Comput Chem*, **31**, 455-461 (2010).
55. Humphrey, W. et al. Vmd: Visual molecular dynamics. *J. Mol. Graph.*, **14**, 33-38, 27-38 (1996).
56. Morris, G. M. et al. Autodock4 and autodocktools4: Automated docking with selective receptor flexibility. *J. Comput. Chem.*, **30**, 2785-2791 (2009).
57. Xie, Y. et al. A novel electrochemical microfluidic chip combined with multiple biomarkers for early diagnosis of gastric cancer. *Nanoscale Res Lett.*, **10**, 9 (2015).

Supplementary Files

This is a list of supplementary files associated with this preprint. Click to download.

- [SupplementaryInformation.docx](#)